TROPICAL CYCLONE RESEARCH REPORT
TCRR **76**: 1–11 (2020)
Meteorological Institute
Ludwig Maximilians University of Munich

Solutions of the Eliassen balance equation for inertially and/or symmetrically stable and unstable vortices

Shanghong Wang[a], Michael T. Montgomery[b1] and Roger K. Smith[a]
[a] *Meteorological Institute, Ludwig-Maximilians University of Munich, Munich, Germany*
[b] *Dept. of Meteorology, Naval Postgraduate School, Monterey, CA*

Abstract:
Two methods for solving the Eliassen equation for the corresponding balanced secondary circulation of a numerically-simulated, high-resolution tropical cyclone vortex are compared. In idealized calculations for a symmetrically stable vortex, both methods (successive over-relaxation and multi-grid) converge and the solutions are broadly similar. In more typical cases, where the vortex has regions of inertial or symmetric instability, it is necessary to coarsen the data from the numerical simulation to determine the balanced secondary circulation. A convergent solution can be obtained with the multi-grid method for a finer grid spacing than with the SOR method. However, the multi-grid method fails to converge when the vertical grid spacing is similar to that of the numerical simulation. Results using both methods confirm the inability of the balance formulation in capturing the strong inflow and resulting tangential wind spin up in the frictional boundary layer during a period of rapid intensification.
Typical tropical cyclone simulations show an inflow layer just beneath the upper-level outflow layer and the corresponding balanced secondary circulation may show such an inflow layer also. However, caution is called for in attributing this inflow layer to a balanced flow response driven by the distribution of diabatic heating and tangential momentum forcing. Our study suggests that it is likely an artifact of the *ad hoc* regularization procedure that is necessary to keep the Eliassen equation globally elliptic in regions of inertial and/or symmetric instability.

KEY WORDS hurricane; tropical cyclone; typhoon

Date: August 11, 2020; Revised ; Accepted

1 Introduction

For a slowly evolving tropical cyclone vortex in which flow asymmetries are not a dominant factor, a well known approximate description of the slow evolution is furnished by the Eliassen balance vortex model (Willoughby 1979; Shapiro and Willoughby 1982, Schubert and Hack 1982, Smith et al. 2018 and refs.). In this reduced model, the tropical cyclone vortex is represented to leading order by the primary (tangential) circulation the cyclone centre. Superposed on the primary circulation is a secondary (overturning) circulation, which is typically inwards in the lower troposphere and outwards in the upper troposphere. The secondary circulation is driven primarily by the aggregate of latent heat release in deep cumulus convection in the central convection zone of the vortex.

Assuming the tropical cyclone is in strict gradient and hydrostatic balance, the secondary circulation can be diagnosed by solving a partial differential equation in the radius-height plane for the meridional streamfunction (the so-called Eliassen equation for the transverse circulation). This equation governs the overturning circulation that is required to keep the vortex in a state of persistent thermal wind balance as the tangential momentum forcing and thermodynamic heat forcing tries to drive the vortex out of balance. Previous work has suggested that this balance model is sufficient to describe the secondary circulation in an intensifying tropical cyclone, including in the vortex boundary layer (Heng et al. 2017). However, this assertion has been rebutted by Montgomery and Smith (2018), who noted, *inter alia*, that Heng et al. did not solve a strictly balance vortex model and inadvertently ignored the derivational requirement that the basic state vortex remain in a state of strict thermal wind balance during the vortex evolution.

Heng et al. (2018) attempted to rebut the critique of Montgomery and Smith (2018) by solving the Eliassen equation for a single numerical simulation, but again employed basic state vorticies that are not in strict thermal wind balance. Recent work of Montgomery and Persing (2020) has affirmed prior findings of Bui et al. (2009), Abarca and Montgomery (2014) and demonstrated that the strict Eliassen balance model fails to represent the strong inflow in the boundary layer needed to generate the intensifying tangential winds.

Most previous solutions of the Eliassen equation have been obtained using the successive over-relaxation (SOR) method including those in the aforementioned papers.

[1]Correspondence to: Prof. M. T. Montgomery, Department of Meteorology, Naval Postgraduate School, Monterey, CA USA. E-mail: mtmontgo@nps.edu

Recent work by Wang et al. (2020) using a particularly high spatial resolution simulation of an intensifying tropical cyclone has found that balance solutions can be obtained only by using a coarsened resolution representation of the simulated vortex. This work affirms and underscores the findings of Montgomery and Persing (2020) and raises a new question of whether axisymmetric balance dynamics is robustly meaningful in high resolution simulations of tropical cyclone intensification. By robustly meaningful we mean that a solution actually exists. A particular problem is that, as shown by Smith et al. (2018), the evolution of a vortex in a balanced formulation develops regions of inertial instability in which the Eliassen equation becomes hyperbolic. In an attempt to overcome this problem, it is necessary to modify the coefficients of the Eliassen equation in these regions so that the equation remains globally elliptic. The procedure for carrying out this modification, often referred to as *regularization*, is necessarily *ad hoc*. Even if a mathematical solution of the regularized Eliassen equation could be shown to exist, an extensive region of regularization may be a reason for the SOR method to fail, unless the resolution of the model data in the Eliassen equation are coarsened.

As a first step in verifying the robustness of their findings, Wang et al. used an independent multi-grid solution method for solving the Eliassen equation. The purpose of this study is threefold: (1) to document the details of the computational methods used in Wang et al. (2020); (2) to explore the sensitivity of the solutions to the particular method used; and (3) to assess the robustness of conclusions based on the SOR method. A specific question addressed is whether a convergence solution of the Eliassen equation for a high-resolution simulation can be obtained using a multi-grid method when the straightforward SOR method fails.

We describe the Calculation configuration in section 2 and review briefly the SOR method and the more sophisticated multi-grid method in section 3. The results of various calculations are presented in section 4. The conclusions are presented in section 5.

2 The calculations

In axisymmetric cylindrical coordinates (r, z), the Eliassen equation for the streamfunction ψ of the secondary circulation has the following form (as in Montgomery and Persing 2020),

$$\frac{\partial}{\partial r}\left[\bar{A}\frac{\partial\psi}{\partial r}+\frac{1}{2}\bar{B}\frac{\partial\psi}{\partial z}\right]+\frac{\partial}{\partial z}\left[\bar{C}\frac{\partial\psi}{\partial z}+\frac{1}{2}\bar{B}\frac{\partial\psi}{\partial r}\right]=\dot{\Theta}, \quad (1)$$

where,

$$\bar{A}=-g\frac{\partial\chi}{\partial z}\frac{1}{\rho r}=\left(\frac{\chi}{\rho r}\right)N^2, \quad (2)$$

$$\bar{B}=-\frac{2}{\rho r}\frac{\partial}{\partial z}(\chi C)=-\frac{2}{\rho r}\left(\chi\xi\frac{\partial v}{\partial z}+C\frac{\partial\chi}{\partial z}\right), \quad (3)$$

$$\bar{C}=\left(\xi(\zeta+f)\chi+C\frac{\partial\chi}{\partial r}\right)\frac{1}{\rho r}=\frac{\chi}{\rho r}I_g^2, \quad (4)$$

and

$$\dot{\Theta}=g\frac{\partial}{\partial r}\left(\chi^2\dot{\theta}\right)+\frac{\partial}{\partial z}\left(C\chi^2\dot{\theta}\right)+\frac{\partial}{\partial z}\left(\chi\xi\dot{V}\right), \quad (5)$$

where v is the tangential velocity components(denotes the azimuthal wavenumber zero flow component), $\chi=1/\theta$ is the inverse of the potential temperature, $C=v^2/r+fv$ is the sum of centrifugal and Coriolis forces per unit mass, $\xi=f+2v/r$ is twice the local absolute angular velocity, f is the Coriolis parameter (assumed constant) and g is the acceleration due to gravity. $\zeta=(1/r)\partial(rv)/\partial r$ is the vertical component of relative vorticity, N^2 is the square of the Brunt-Väisälä frequency, defined as $(g/\theta)\partial\theta/\partial z$, and $I_g^2=\xi(\zeta+f)+(C/\chi)\partial\chi/\partial r$ is the square of the generalized inertial frequency. The quantities $\bar{A}$ and $\bar{C}$ are proportional to the static stability and inertial stability, respectively. The quantity $\bar{B}$ characterizes, in part, the strength of the vertical shear of the gradient wind. The forcing term $\dot{\Theta}$ represents a combination of the diabatic heating and momentum forcing, $\dot{\theta}$ and $\dot{V}$ respectively, defined as follows

$$\dot{\Theta}=g\frac{\partial}{\partial r}\left(\chi^2\dot{\theta}\right)+\frac{\partial}{\partial z}\left(C\chi^2\dot{\theta}\right)+\frac{\partial}{\partial z}\left(\chi\xi\dot{V}\right). \quad (6)$$

In the anelastic approximation, the transverse velocity components u and w are given in terms of ψ by:

$$u=-\frac{1}{r\rho}\frac{\partial\psi}{\partial z}, \qquad w=\frac{1}{r\rho}\frac{\partial\psi}{\partial r}. \quad (7)$$

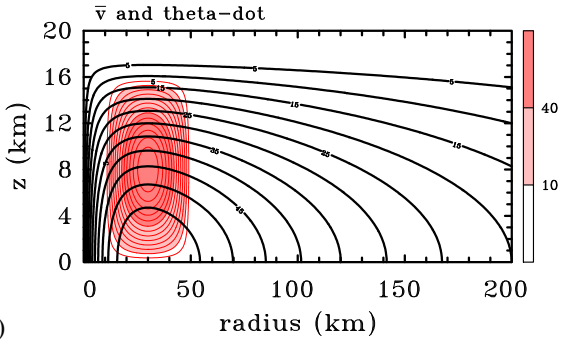

(a)

Figure 1. The idealized tropical-cyclone-like vortex to a prescribed diabatic heating rate in Calc-A. Shown as contours of tangential velocity (black thick contour interval 5 m s^{-1}) and prescribed diabatic heating, $\dot{\theta}(r, z)$ (shaded, contour interval 5 K per hour).

Four sets of calculations are carried out to compare the balanced solutions for the streamfunction of the secondary circulation of tropical-cyclone-like flows obtained using the SOR and multigrid solution methods.

The first set of calculations, referred to as Calc-A, relate to the balanced streamfunction of an idealized

tropical-cyclone-like vortex defined by a specified tangential wind profile, $v(r,z)$, forced by a specified distribution of diabatic heating rate $\dot{\theta}(r,z)$, where

$$v(r,z) = V_m(\frac{r}{r_m})exp[\frac{1}{b}(1-(\frac{r}{r_m})^b)]\cos(\frac{\pi z}{2z_d}), \quad (8)$$

with b = 0.45, V_m = 60 m s^{-1}, r_m = 30 km, z_d =18 km, and

$$\begin{aligned}\dot{\theta}(r,z) &= \dot{\Theta}cos(\frac{1}{2}\pi\frac{\delta r}{r_w})\cos(\frac{1}{2}\pi\frac{\delta z}{z_c}) \qquad (r<r_c)\\ &= \dot{\Theta}\cos(\frac{1}{2}\pi\frac{\delta r}{r_w})\cos(\frac{1}{2}\pi\frac{\delta z}{z_c}) \qquad (r>r_c) \quad (9)\end{aligned}$$

with $\delta r = r - r_c$, $\delta z = z - z_c$, r_c = 30 km, z_c = 8 km and r_w = 20 km. In these formulae: V_m is the maximum tangential wind speed, which occurs at the surface at radius r_m; r_c and z_c are the radius and height of the maximum diabatic heating; $\dot{\Theta}$ = 70 K h^{-1} is the maximum amplitude of the heating rate, r_w is the width of the heating function which is 20 km. The tangential wind decreases sinusoidally with height to an altitude of z_d =18 km and is set to zero above 18 km. There is no momentum forcing in these particular calculations. The prescribed structure of tangential wind and diabatic heating is shown in Fig. 1.

The set of calculations, Calc-B, relate to the balanced secondary circulation at 60 h of the simulation in Wang et al. (2020). The tangential wind field is azimuthally-averaged and time-averaged for one hour using 1 minute output data and the corresponding balanced pressure and temperature distribution are obtained by using the unapproximated method of Smith (2006), assuming a latitude of 20^{o}N and the Dunion moist tropical sounding (Dunion 2011) at some large radius. The original horizontal grid spacing is 1 km from the model output and there are 78 vertical levels from 0 km to 25 km. The vertical grid spacing is 100 m in the first 1 km and 500 m from16 km to 25 km. Between 1 km and 16 km, the vertical grid spacing is uniformly stretched.

The set of calculations, Calc-C, relate to the balanced secondary circulation of the vortex structure in Wang et al. (2020) at 60 h. but with the prescribed diabatic heating rate in Calc-A, while the set of calculations Calc-D relate to the balanced secondary circulation of the vortex structure in Calc-A, but with the diabatic heating and momentum forcing in Wang et al. (2020) at 60 h. The full set of calculations is summarized in Table I.

Calculation	vortex	forcing
Calc-A	ideal	ideal
Calc-B	model	model
Calc-C	model	ideal
Calc-D	ideal	model

Table I. Summary of all calculations

Each set of calculations is performed with the SOR and multi-grid method with different radial and/or vertical resolution. To meet the special requirements of the multi-grid method in relation to the number of grid points, the computational domain of each case consists of a cylindrical region 256 km in radius and 19.2 km in height.

Table II shows the number of non-elliptic points in Calc-B and Calc-C. It is clear that, the number of non-elliptic grid points increases with decreasing grid spacing. Figure 2 shows that the negative discriminant area is broader at the finest resolution (panel (b)) than at the coarsest resolution (panel (a)), especially in the upper-troposphere. Furthermore, the regions of static and symmetric instability are somewhat more extensive in the upper-troposphere. It is foreseeable that the increase in negative discriminant area in the case of higher resolution might lead to additional difficulty in solving the Eliassen equation.

Non-elliptic	dz = 600 m	dz = 300 m	dz = 150 m
dr = 2 km	558	1273	2517
dr = 1km	1119	2559	5064

Table II. Number of non elliptic points in Calc-B and Calc-C for different radial and vertical grid spacings, dr and dz, respectively.

3 Solution methods

3.1 Successive over-relaxation method

On the discrete (r,z) mesh of points, the solver iterates for ψ by linearly marching through the grid mesh and minimizing the residual R defined by

$$R = \bar{A}\delta_{rr}\psi + \bar{B}\delta_{rz}\psi + \bar{C}\delta_{zz}\psi + \bar{D}\delta_r\psi + \bar{E}\delta_z\psi - \dot{\Theta}. \quad (10)$$

Here, the operator δ represents a discrete partial derivative in the direction of the subscript, with second-order derivatives having subscripts. The streamfunction at iteration step $k+1$ is obtained from that at step k by successive over-relaxation:

$$\psi_{k+1} = \psi_k + \frac{\omega R_k}{2}\left[\frac{\bar{A}}{(\Delta r)^2} + \frac{\bar{C}}{(\Delta z)^2}\right]^{-1} \quad (11)$$

where $\bar{A}$, $\bar{B}$, $\bar{C}$ and $\dot{\Theta}$ are defined in Section 2,

$$\bar{D} = \frac{\partial \bar{A}}{\partial r} + \frac{1}{2}\frac{\partial \bar{B}}{\partial z}, \quad (12)$$

$$\bar{E} = \frac{1}{2}\frac{\partial \bar{B}}{\partial r} + \frac{\partial \bar{C}}{\partial z}, \quad (13)$$

and $\omega = 1.8$ is the empirically chosen over-relaxation parameter (generally between 1.0 and 2.0). The iteration is deemed to have converged if the maximum difference in ψ between two iteration steps is less than 10^{-8} times the maximum magnitude of the solution at all interior (r,z) grid points. This criterion follows the suggestion of Adams 1991 in his multi-grid method. Other technical details of the method can be found in Press et al. (1992) page 866–870.

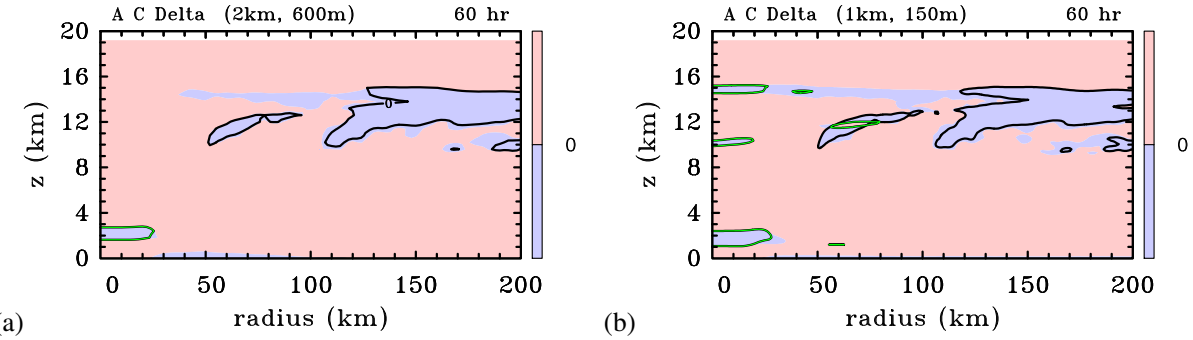

Figure 2. Sign of the coefficients $\bar{A}$, $\bar{C}$ and the discriminant $D = 4\bar{A}\bar{C} - \bar{B}^2$ in the Eliassen equation (1) for Calc-B and Calc-C with (a) dr = 2 km, dz = 600 m and (b) dr = 1 km, dz = 150 m.. The quantities $\bar{A}$ and $\bar{C}$ are proportional to the static stability and inertial stability, respectively, while the quantity $\bar{B}$ characterizes, in part, the strength of the vertical shear of the gradient wind. $\bar{A}$ (zero lines as green), $\bar{B}$ (zero lines as black) and D (shaded, blue for negative, red for positive).

3.2 Multi-grid method

The multi-grid method is an iteration method that has become quite popular and versatile for solving linear elliptic partial differential equations and even some nonlinear problems (Adams 1991). Although the method is not an over-relaxation method in the traditional sense, the method takes advantage of the fact that the residual error damps more quickly on small scales than larger scales of the grid mesh. The difference in error attenuation between the small and large scales allows one to cycle between small-scale and large scale grids in order to accelerate the convergence rate of the solution. Specifically, the fine grid is used to eliminate the high-frequency oscillation error; the elimination of the low-frequency oscillation error is accomplished by the coarser grids and the coarse-grid solution is then projected back onto the fine grid and the cycle is repeated and so on until the residual decreases to a given error criterion. Because the convergence speed of the low-frequency oscillation error in the coarse grid is faster than on the original grid, the multi-grid method is generally much faster than other classical, one-scale, iteration methods, such as SOR, Gauss-Siedel or Jacobi iteration. The computational efficiency of the multi-grid method is generally very high because the method scales in proportion to the number of grid points of the mesh. An excellent tutorial on multi-grid methods and their relation to the classical one-scale iteration methods is provided by Briggs et al. 2000.

In the implementation of the multi-grid method method herein, the same convergence criterion is employed as for the SOR method discussed above.

4 Results

4.1 Calculation set Calc-A

This set of twelve calculations Calc-A comprise six using the SOR method and six using the multi-grid method with a combination of $dr = 1$ km or 2 km and $dz = 150$ m, 300 m,.or 600 m. Figure 3 shows radial and vertical velocity components structure for a selection of these calculations. The 1 km radial grid spacing corresponds to the spacing in the model simulation used to generate the data for Calc-B. The panels in the left column show the solutions using the multi-grid method and the right columns show those using the SOR method. From the figure it is seen that the flow in all panels is essentially the same, confirming the integrity of both solution methods.

The maximum inflow occurs near the surface while the maximum outflow occurs at a height of about 15 km. The strongest ascent occurs in the region of maximum heating, a feature to be expected from the study of Shapiro and Willoughby (1982) and Smith et al. (2018). The maximum inflow for each of the 12 cases differs by no more than 0.2 m s^{-1} and the maximum outflowdiffers by no more than 0.1 m s^{-1}. In essence, for this idealized case, the multi-grid and SOR methods give essentially the same results, irrespective of grid spacing.

4.2 Calculation set Calc-B

We turn now to examine in more depth the solutions for the balanced secondary circulation in the high-resolution tropical cyclone simulation presented by Wang et al. (2020) forced by the azimuthally averaged diabatic heating and tangential momentum forcing (including the eddy terms) diagnosed from the simulation at 60 h. These forcing distributions are shown in figures 9b,c of Wang et al. (2020). Table III shows that, as the resolution increases, convergence solutions become harder to obtain. Figure 4 compares solutions for the balanced secondary circulation with different grid resolutions with that obtained from the azimuthally averaged output from the simulation, itself, at 60 h. Figure 4a shows the azimuthally-averaged circulation in the simulation while Figure 4b shows the corresponding balanced solution obtained using the SOR method with a radial grid spacing of 2 km and vertical grid spacing of 600 m This choice of grid configuration is coarser than that used for the simulated vortex for reasons discussed in the Introduction.

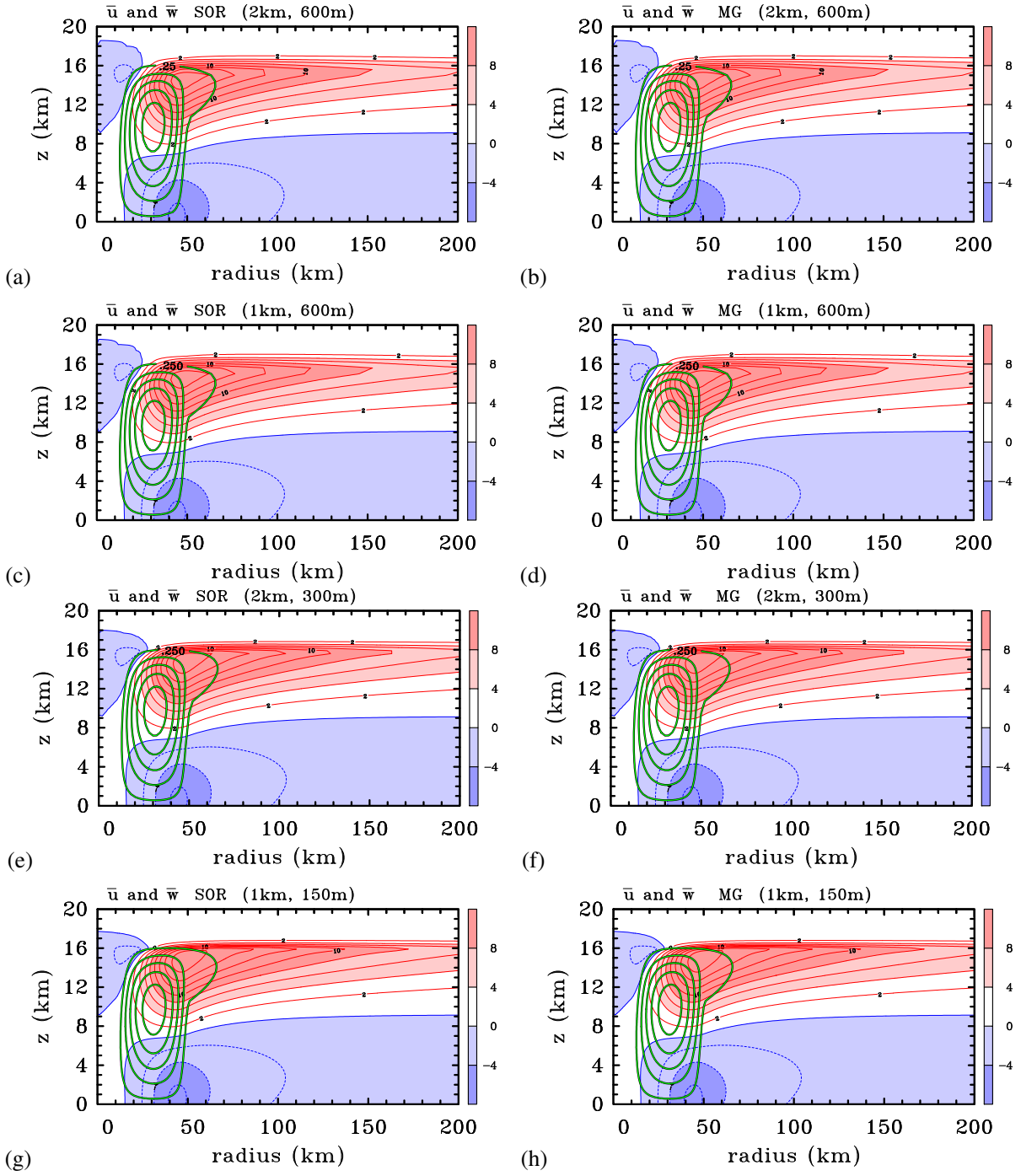

Figure 3. Axisymmetric balanced solutions for the radial ($\bar{u}$) and vertical ($\bar{w}$) components of the secondary circulation in a subset of Calc-A. The calculations differ in the method of solution (left columns SOR, right columns multigrid) and the radial and vertical grid spacing (dr, dz): (a) and (b) $dr = 2$ km, $dz = 600$ m; (c) and (d) $dr = 1$ km, $dz = 600$ m; (e) and (f) $dr = 2$ km, $dz = 300$ m; (g) and (h) $dr = 1$ km, $dz = 150$ m. Contour interval for $\bar{u}$: 2 m s^{-1} when $\bar{u} > 0$, 1 m s^{-1} when $\bar{u} < 0$. Positive contours solid, negative contours dashed. Shading values indicated on color bar. Green thick contours are shown for $\bar{w}$: 0.25 m s^{-1} (Only positive values are shown).

As noted by Wang et al. (2020), the mean height of the balanced outflow is too low (12 km compared with 14 km) and the outflow is split at larger radii in the balanced solution. There are strong discrepancies also in the strength and radial extent of the inflow layers. For example, the inflow below the outflow layer is approximately twice as strong in the balanced solution and the inflow layer above the outflow layer is barely evident. The maximum radial velocity in the upper level outflow in the balance solution is 23.3 m s^{-1} compared with 20.3 m s^{-1} in the simulation. The boundary layer inflow in the balance solution is significantly weaker than in the simulation

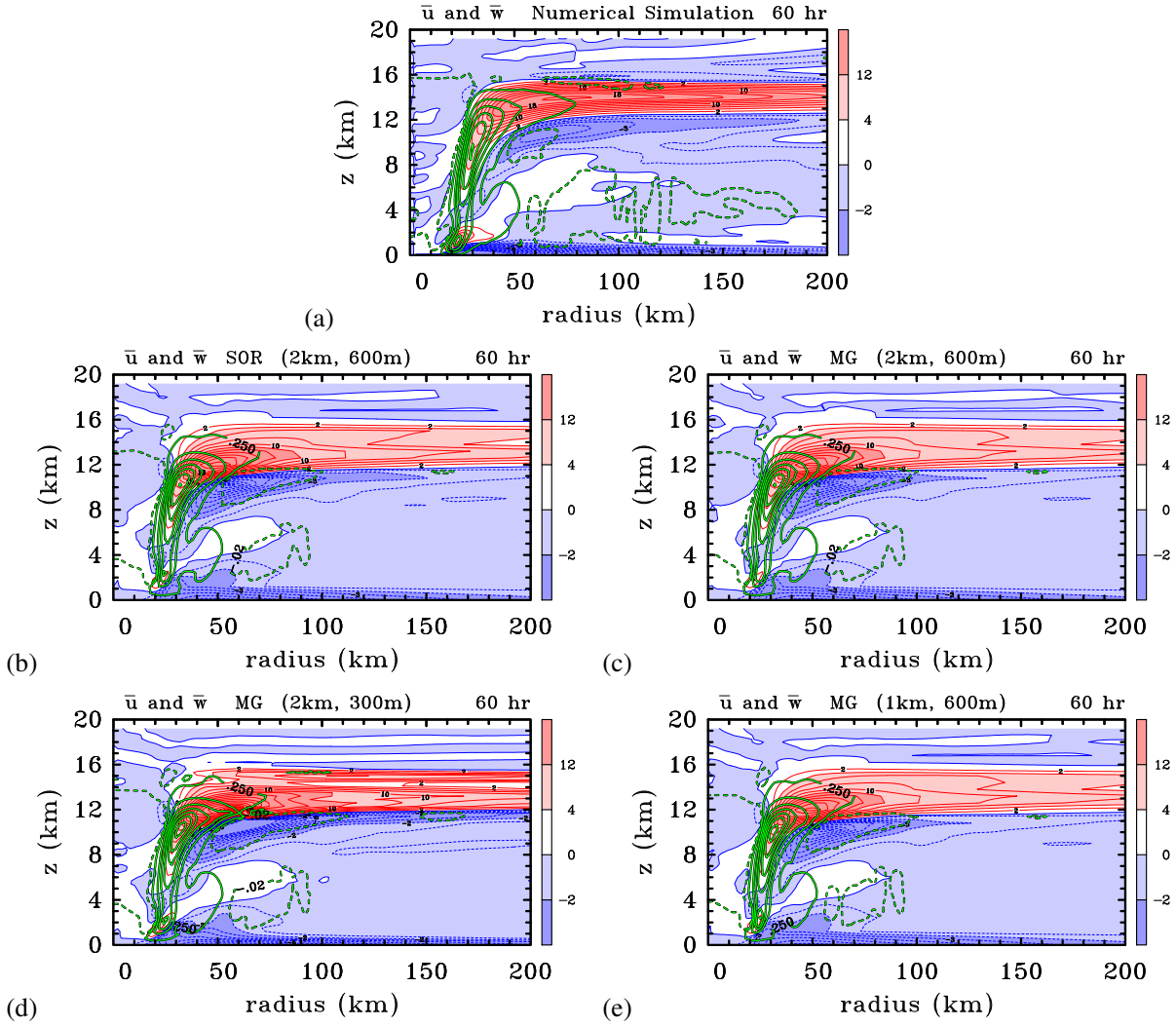

Figure 4. Axisymmetric balanced solutions for the radial ($\bar{u}$) and vertical ($\bar{w}$) components of the secondary circulation at 60 h in the numerical simulation (panel (a)) and in a subset of axisymmetric balanced solutions for Calc-B. The fields in panels (a) are azimuthally-averaged and time-averaged for one hour using 1 min output. (b) SOR and (c) multi-grid with $dr = 2$ km, $dz = 600$ m. (e) multi-grid with $dr = 2$ km, $dz = 300$ m; (f) multi-grid with $dr = 1$ km, $dz = 600$ m. Contour interval for 2 m s^{-1} when $\bar{u} > 0$, 1 m s^{-1} when $\bar{u} < 0$. Positive contours solid, negative contours dashed. Shading values indicated on color bar. Only two thick contours are shown for $\bar{w}$. For $\bar{w} > 0$, 0.25 m s^{-1} (green, solid); for $\bar{w} < 0$, -0.02 m s^{-1} (green, dashed). Shading values indicated on colour bar.

(maximum inflow 7.5 m s^{-1} compared with 24.5 m s^{-1}, a factor of three discrepancy), but is much deeper in the inner region as found by Montgomery and Persing (2020).

Figure 4c shows the balance solution using the multi-grid method with the same grid configuration as in Figure 4b. Comparing Figures 4b and 4c it is seen that the multi-grid solution is almost the same as that obtained with SOR. Indeed, the maximum upper-level outflow and inflow have comparable values (Table IV), but the outflow and inflow weaken slightly faster with radius with the multi-grid method. Again, the boundary layer inflow in the balance solution is much weaker than in the numerical simulation, reflecting the fact that the balance assumption in the boundary layer is poor.

When the vertical grid spacing is halved, the SOR method failed to converge, but a convergent solution is still possible using the multi-grid method (Figure 4d). However, this solution is significantly different in detail from that with the coarser vertical resolution in Figure 4c. The outflow layer has a stronger maximum and has a more obvious two-layer structure at large radii. The upper inflow is stronger also and extends to a larger radius, even exceeding the strength of that in the numerical simulation. Although the maximum boundary layer inflow is larger also, its strength is still greatly underestimated relative to that of the simulation. When the vertical grid spacing is halved again to 150 m, neither solution methods converge (Table III).

When the radial grid spacing is reduced to 1 km, the same as in the numerical simulation (Figure 4e), a convergent solution is possible only using the multi-grid method and only then using the coarsest vertical grid

spacing of 600 m. The solution in this case is virtually indistinguishable from that in Figure 4c. These findings support that of Wang and Smith (2019), Wang et al. (2020) and Montgomery and Persing (2020) indicating that the balance solution has intrinsic limitations in diagnosing the secondary circulation of the numerical simulation.

Calc-B	SOR	MG
dr = 2 km, dz = 600 m	solvable	solvable
dr = 2 km, dz = 300 m	unsolvable	solvable
dr = 2 km, dz = 150 m	unsolvable	unsolvable
dr = 1 km, dz = 600 m	unsolvable	solvable
dr = 1 km, dz = 300 m	unsolvable	unsolvable
dr = 1 km, dz = 150 m	unsolvable	unsolvable

Table III. Summary of SOR and multi-grid performance for Calc-B.

Calc-B	upper-max	upper-min	lower-min
Simulation	20.3 m/s	-4.9 m/s	-24.5 m/s
SOR, 2 km, 600 m	23.3 m/s	-10.2 m/s	-7.5 m/s
MG, 2 km, 600 m	22.8 m/s	-9.7 m/s	-7.5 m/s
MG, 2 km, 300 m	38.9 m/s	-14.8 m/s	-9.2 m/s
MG, 1 km, 600 m	22.8 m/s	-9.7 m/s	-7.5 m/s

Table IV. Maximum values of inflow and outflow for each case in Calc-B.

4.3 Calculation set Calc-C

In an effort to pinpoint the reasons for the failure of the SOR and multi-grid methods to converge for lower grid spacings in calculation set Calc-B, we turn first to a set of calculations with the same vortex structure in Calc-B, but with the idealized forcing used in Calc-A. The tangential wind structure and prescribed diabatic heating rate used in Calc-C are shown in Figure 5a. As in Calc-B, there are regions where the discriminant of the Eliassen equation is negative (Figure 2) and the equation requires regularization. Even though the diabatic heating rate in these calculations has a regular shape, the secondary circulation has more structure than in Figure 3 with an inflow layer beneath the upper-level outflow.

The two solutions with the same grid spacing are similar with two local maxima in the upper-level outflow (Figure 5b,c). However, the multi-grid solution with the same radial grid spacing, but a vertical grid spacing of 300 m has three local maxima within the outflow layer and a much stronger upper level inflow (Figure 5d). As in Calc-B and as detailed in Table V, the SOR method does not converge with a 300 m vertical grid spacing and neither solution method converges with a 150 m vertical grid spacing.

When the radial grid spacing is reduced to 1 km, it is only possible to obtain a solution with the multi-grid method and only then with a vertical grid spacing of 600 m. This solution, which is shown in Figure 5e, is virtually the same as the solution with a 2 km radial grid spacing in Figure 5b. This result suggests that the solution is less sensitive to changes in the radial resolution than to changes in the vertical resolution, at least where a convergent solution is possible.

Calc-C	SOR	MG
dr=2km, dz=600m	solvable	solvable
dr=2km, dz=300m	unsolvable	solvable
dr=2km, dz=150m	unsolvable	unsolvable
dr=1km, dz=600m	unsolvable	solvable
dr=1km, dz=300m	unsolvable	unsolvable
dr=1km, dz=150m	unsolvable	unsolvable

Table V. Summary of SOR and multi-grid performance for Calc-C.

4.4 Calculation set Calc-D

The final set of calculations, Calc-D, uses the full diabatic heating and momentum forcing (including that from the eddies) from the numerical simulation (shown in figures 9b,c of Wang et al. 2020), as in Calc-B, but incorporate the idealized vortex structure in Calc-A. The unique feature is that this vortex is everywhere symmetrically stable and the Eliassen equation does not require regularization. The balanced secondary circulation for this set of calculations is shown in Figure 6. The four calculations with 600 m vertical grid spacing and either 1 or 2 km radial grid spacing show similar structures with a hint of a second outflow maximum above the main outflow layer. The second outflow maximum is presumably related to the fine structure of the diabatic heating rate. With a vertical grid spacing of 300 m, the second outflow feature becomes more marked using both solution methods (panels (e) and (f)), while in the finest resolution solutions (panels (g) and (h)), the second outflow structure is even more pronounced.

Notably, there is no concentrated inflow layer below the main outflow layer as in Calc-B and Calc-C. This result indicates that the upper-level inflow layer in Calc-B and Calc-C is mainly a consequence of the need to regularize the coefficients of the Eliassen equation in regions of symmetric instability. The implications of this finding are discussed in the next section.

As shown in Table VI, when the resolution increases, flow extrema increase marginally. For the case of the same resolution, both two solution methods give essentially the same results. Most importantly, without the need to regularize the Eliassen equation, a convergent solution can be obtained using both solution methods.

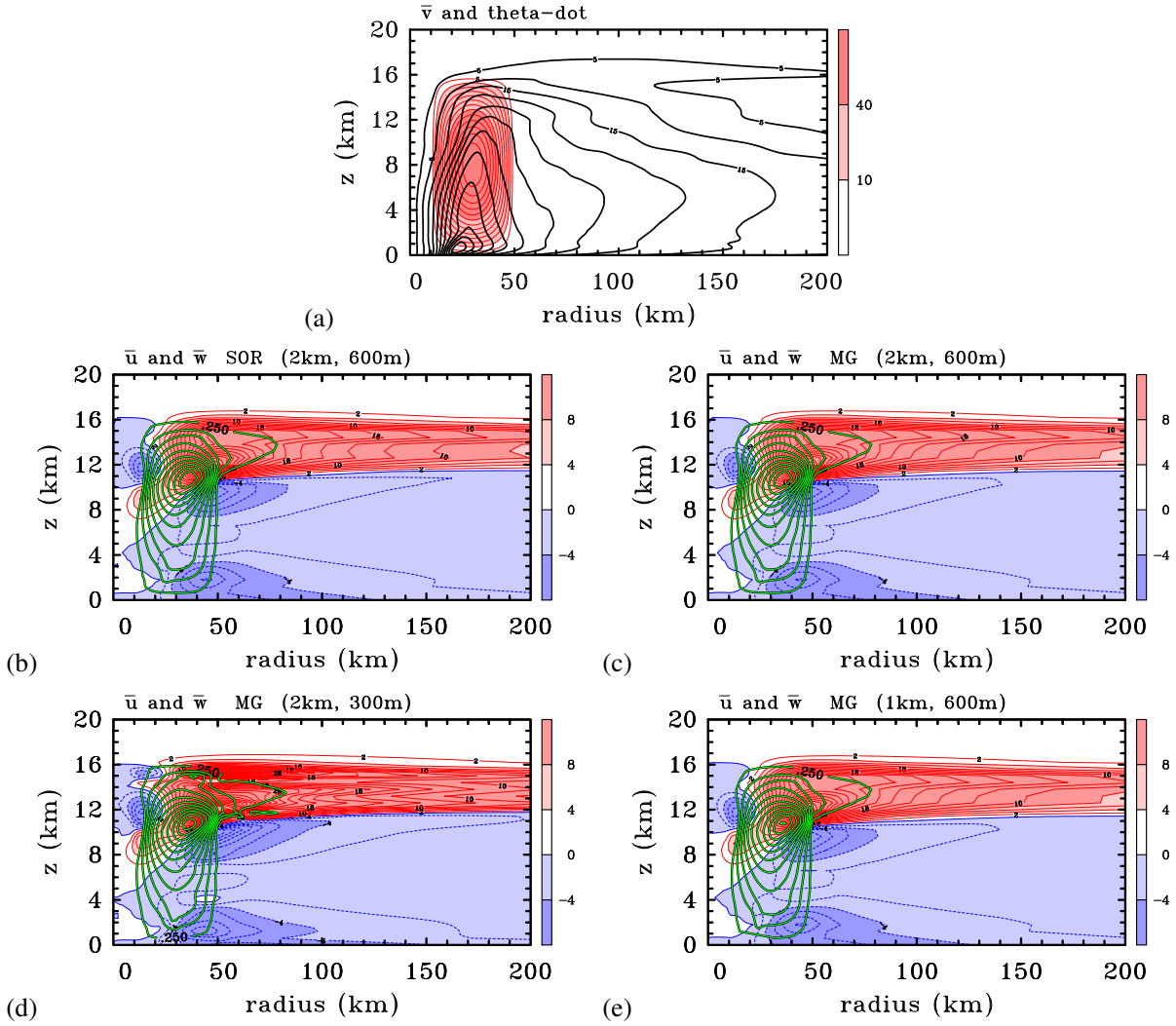

Figure 5. Axisymmetric balanced solutions for the radial ($\bar{u}$) and vertical ($\bar{w}$) components of the secondary circulation in a subset of Calc-C. For comparison, panel (a) shows the tangential wind from the numerical simulation at 60 h and a prescribed diabatic heating rate (K per hour). (b) SOR method, $dr = 2$ km, $dz = 600$ m. Panels (c)-(e) use the multi-grid method with (c) $dr = 2$ km, $dz = 600$ m; (d) $dr = 2$ km, $dz = 300$ m; (e) $dr = 1$ km, $dz = 600$ m. Contour interval for $\bar{u}$: 2 m s^{-1} when $\bar{u} > 0$, 1 m s^{-1} when $\bar{u} < 0$. Positive contours solid, negative contours dashed. Shading values indicated on color bar. Green thick contours are shown for $\bar{w}$: 0.25 m s^{-1} (Only positive values are shown).

4.5 Summary of the calculations

Taken together, the four sets of calculations described above indicate that the ability to obtain a convergent solution of the Eliassen equation for the balanced secondary circulation of a high-resolution simulated tropical cyclone is severely compromised by the presence of regions where the azimuthal flow is inertially and/or symmetrically unstable. Such regions are predominantly found in the upper troposphere (see e.g. Smith et al. 2018). By severely compromised, we mean that it is no longer possible to obtain a convergent solution at a resolution commensurate with that of the simulation. In these situations, it is possible to obtain a convergent solution only by coarsening the grid, which serves to shrink the region of instability. With this coarsening, the solutions obtained by the SOR and multi-grid methods are essentially the same, but in the calculations carried out here, the multi-grid method is capable of obtaining a convergent solution with a smaller radial and/or vertical grid spacing than the SOR method, before it too fails to converge.

Comparison between the two sets of calculations Calc-C and Calc-D suggest that the inflow layer just beneath the upper-level outflow layer in any balance solution is a consequence of the regularization that is required in Calc-C, but not in Calc-D. Because regularization is an *ad hoc* procedure, this result calls for caution in attributing such inflow layers to a balanced flow response driven by the distribution of diabatic heating and tangential momentum forcing. It follows that an explanation of the upper-level inflow layers that are found in numerical simulations of

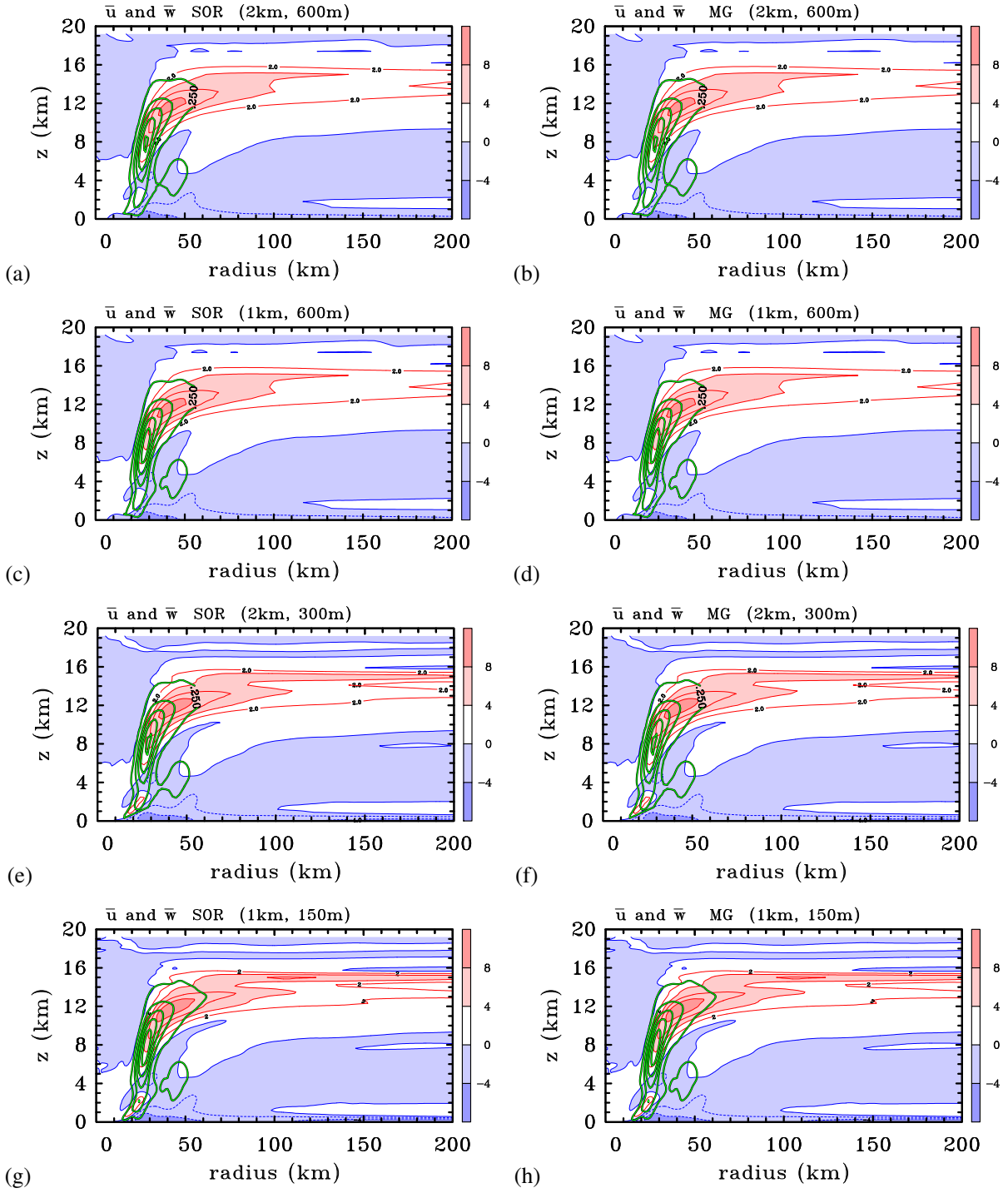

Figure 6. Axisymmetric balanced solutions for the radial ($\bar{u}$) and vertical ($\bar{w}$) components of the secondary circulation in a subset of Calc-D (idealized vortex, generalized diabatic heating (K per hour) and generalized tangential momentum forcing (m s^{-1} per hour). The calculations differ in the method of solution (left columns SOR, right columns multigrid) and the radial and vertical grid spacing (dr, dz): (a) and (b) $dr = 2$ km, $dz = 600$ m; (c) and (d) $dr = 1$ km, $dz = 600$ m; (e) and (f) $dr = 2$ km, $dz = 300$ m; (g) and (h) $dr = 1$ km, $dz = 150$ m. Contour interval for $\bar{u}$: 2 m s^{-1} when $\bar{u} > 0$, 1 m s^{-1} when $\bar{u} < 0$. Positive contours solid, negative contours dashed. Shading values indicated on color bar. Green thick contours are shown for $\bar{w}$: 0.25 m s^{-1} (Only positive values are shown).

tropical cyclones needs to be based on more fundamental considerations than assuming global thermal wind balance (Wang et al. 2020).

The subset of calculations Calc-B that converge affirm prior work of Bui et al. (2009), Abarca and Montgomery (2014), Montgomery and Persing (2020), Wang and Smith 2019 and Wang et al. (2020) in that the boundary layer inflow in the strict axisymmetric Eliassen balance model

Calc-D	outflow	inflow
MG, dr = 2 km, dz = 600 m	8.8 m/s	-5.1 m/s
MG, dr = 1 km, dz = 600 m	8.9 m/s	-5.2 m/s
MG, dr = 2 km, dz = 300 m	9.3 m/s	-5.5 m/s
MG, dr = 1 km, dz = 300 m	9.3 m/s	-5.5 m/s
MG, dr = 2 km, dz = 150 m	9.4 m/s	-5.8 m/s
MG, dr = 1 km, dz = 150 m	9.5 m/s	-5.9 m/s
SOR, dr = 2km, dz = 600 m	8.8 m/s	-5.1 m/s
SOR, dr = 1km, dz = 600 m	8.9 m/s	-5.2 m/s
SOR, dr = 2km, dz = 300 m	9.3 m/s	-5.5 m/s
SOR, dr = 1km, dz = 300 m	9.4 m/s	-5.6 m/s
SOR, dr = 2km, dz = 150 m	9.4 m/s	-5.8 m/s
SOR, dr = 1km, dz = 150 m	9.5 m/s	-5.9 m/s

Table VI. Maximum values of upper-level inflow and outflow for each case in Calc-D.

is far too weak (by a factor of about 3) compared to the simulated inflow in the inner-core region of the vortex. It follows that the Eliassen balance model is unable to represent the nonlinear boundary layer spin up mechanism that is essential for properly capturing the intensification of the maximum tangential wind of an intensifying tropical cyclone when realistic sub grid scale diffusivities are employed consistent with current observational knowledge. These results are further evidence to refute the claim by Heng et al. 2017, Heng et al. 2018 that the balance dynamics is sufficient to capture the secondary circulation of an intensifying tropical cyclone, including the boundary layer.

5 Conclusions

We have compared two solution methods, the SOR-method and a multi-grid method, to solve the Eliassen equation for the balanced secondary circulation of a tropical cyclone vortex to a particular forcing distribution of diabatic heating and tangential momentum forcing. These solutions affirm prior findings concerning the need to coarsen the data from high-resolution numerical simulations in the presence of inertial or symmetric instability when applied to determine the corresponding balanced secondary circulation. They show also that the multi-grid method is able to obtain a convergent solution with a finer grid spacing than the SOR method, although it too fails when the grid spacing is too small. When both methods converge *and the vortex is symmetrically stable*, the solutions are broadly similar.

The calculations suggest that the inflow layer just beneath the upper-level outflow layer in a balance flow solution of the Eliassen equation corresponding to a typical tropical cyclone simulation is a consequence of the need to regularize this equation in regions of inertial and/or symmetric instability. Because regularization is an *ad hoc* procedure, this inference calls for caution in attributing such inflow layers to a balanced flow response driven by the distribution of diabatic heating and tangential momentum forcing. Thus, an explanation of the upper-level inflow layers that are found in numerical simulations of tropical cyclones needs to be based on more fundamental considerations than assuming global thermal wind balance.

Acknowledgement

MTM acknowledges the support of NSF grants AGS-1313948, IAA-1656075, ONR grant N0001420WX01473 and the U.S. Naval Postgraduate School. The views expressed herein are those of the authors and do not represent sponsoring agencies or institutions. S.W. acknowledges a Ph.D. stipend from the China Scholarship Council.

References

Abarca, S. F., and M. T. Montgomery, 2014: Departures from axisymmetric balance dynamics during secondary eyewall formation. *J. Atmos. Sci.*, **71**, 3723–3738.

Adams, J. C., 1991: *MUltigriD Software for Elliptic Partial Differential Equations: MUDPACK (No. 357)*. National Center for Atmospheric Research.

Briggs, W. L., V. E. Hensen, and S. F. McCormick, 2000: *A Multigrid Tutorial, Second Edition*. Society for Industrial and Applied Mathematics, 193 pp., doi:10.1137/1.9780898719505.

Bui, H. H., R. K. Smith, M. T. Montgomery, and J. Peng, 2009: Balanced and unbalanced aspects of tropical-cyclone intensification. *Quart. Journ. Roy. Meteor. Soc.*, **135**, 1715–1731.

Dunion, J. P., 2011: Rewriting the climatology of the tropical north atlantic and caribbean sea atmosphere. *J. Clim.*, **24**, 893–908.

Heng, J., Y. Wang, and W. Zhou, 2017: Revisiting the balanced and unbalanced aspects of tropical cyclone intensification. *J. Atmos. Sci.*, **74**, 2575–2591.

Heng, J., Y. Wang, and W. Zhou, 2018: Reply to comments on revisiting the balanced and unbalanced aspects of tropical cyclone intensification. *J. Atmos. Sci.*, **75**, 2497–2505.

Montgomery, M. T., and J. Persing, 2020: Does balance dynamics well capture the secondary circulation and spin-up of a simulated tropical cyclone? *J. Atmos. Sci.*, **77**, in revision.

Montgomery, M. T., and R. K. Smith, 2018: Comments on: "Revisiting the balanced and unbalanced aspects of tropical cyclone intensification". *J. Atmos. Sci.*, **75**, 2491–2496.

Press, W. H., S. A. Teukolsky, W. T. Vetterling, and B. P. Flannery, 1992: *Numerical Recipes in C: The art of scientific computing*. Cambridge University Press, Cambridge, England, ISBN-13:978-1107404083, 994pp.

Schubert, W. H., and J. J. Hack, 1982: Inertial stability and tropical cyclone development. *J. Atmos. Sci.*, **39**, 1687–1697.

Shapiro, L. J., and H. Willoughby, 1982: The response of balanced hurricanes to local sources of heat and momentum. *J. Atmos. Sci.*, **39**, 378–394.

Smith, R. K., 2006: Accurate determination of a balanced axisymmetric vortex. *Tellus A*, **58**, 98–103.

Smith, R. K., M. T. Montgomery, and H. Bui, 2018: Axisymmetric balance dynamics of tropical cyclone intensification and its breakdown revisited. *J. Atmos. Sci.*, **75**, 3169–3189.

Wang, S., and R. K. Smith, 2019: Consequences of regularizing the Sawyer-Eliassen equation in balance models for tropical cyclone behaviour. *Quart. Journ. Roy. Meteor. Soc.*, **145**, 3766–3779.

Wang, S., R. K. Smith, and M. T. Montgomery, 2020: Upper-tropospheric inflow layers in tropical cyclones. *Quart. Journ. Roy. Meteor. Soc.*, **146**, xx–xx.

Willoughby, H. E., 1979: Forced secondary circulations in hurricanes. *J. Geophys. Res.*, **84**, 3173–3183.